The Institute of Space and Astronautical Science
Report SP No. 17 March 2003

Study for Dynamically Unstable Motion of Reentry Capsule

By

Takashi ABE*†, Syunichi SATO*, Yutaka MATSUKAWA*,
Kazushi YAMAMOTO†, and Kazumi HIRAOKA‡

(1 February 2003)

Abstract: The dynamic stability of the reentry capsule configuration was investigated both experimentally and numerically. The dynamically unstable behavior was observed especially at transonic regime while, at subsonic regime, an intermittent unstable behavior was observed even though an oscillation amplitude is small compared with the one at transonic regime. At supersonic regime, the dynamically unstable behavior observed at transonic regime disappears. At transonic regime, the limit cycle oscillation was observed as a result of the dynamic instability. The results of both the experiment and the numerical simulation show a reasonable agreement. The dynamic pitching moment during the oscillation was modeled for the front and rear part, separately. It is shown that the pitching moment during the oscillation can be evaluated by considering the dynamic effect on the static aerodynamic characteristics. Based on the modeled pitching moment, a theory for the dynamical instability is proposed, which gives not only the growth rate of the oscillation but also the limit cycle oscillation amplitude. According to the theory, the primary cause for the dynamic instability is the dynamical part of the pitching moment at the rear part of the capsule, which is generated by the vortical flow behind the capsule. The dynamical part of the pitching moment at the front part of the capsule works as a stabilizer. Both the growth rate and the limit cycle oscillation suggested by the theory shows a reasonable agreement with the experiment and the numerical simulation.

1. INTRODUCTION

In a planetary exploration, a probe entering into a planetary atmosphere is inevitable in order to deliver scientific instrument on the planetary surface. This is also the case for a sample return mission in which a soil sample of other planet is to be brought back to earth. Such a probe, which often has a capsule configuration of blunted cone, suffers an unstable attitude motion at transonic speed before a parachute deployment. Avoidance of such unstable attitude motion is, besides the heat-shield design, one of key design points for such a reentry capsule

* The Institute of Space and Astronautical Science, Yoshinodai 3-1-1, Sagamihara, Kanagawa 229-8510, Japan.
† University of Tokyo, Hongo, 7-3-1, Bunkyo-ku, Tokyo 113-8656, Japan.
† Kitakaname 1117, Hiratuka, Kanagawa 259, Japan.

since, in the worst case, the capsule may be tumbled out due to this phenomenon, and the mission may be failed. Even though many researchers have attacked this problem [1–6], no clear understanding has yet been obtained for the phenomenon and, currently, such a capsule must be designed on a try-and-error basis.

Recently Hiraki[7] conducted a wind tunnel experiment using a scaled model of the reentry capsule, which was designed so that it can move freely with a one-degree of freedom pitching motion on a tip of the sting type strut. He showed that the pitching motion was dynamically unstable at a transonic speed; that is, the pitching motion is enhanced from a negligibly small amplitude of oscillation and is saturated at a finite amplitude oscillation. At a subsonic speed, however, the unstable pitching motion was not enhanced monotonously to a finite amplitude oscillation but showed an intermittent behavior. At a supersonic speed, such a unstable motion was not observed. He also suggested that the main cause of the phenomenon can be attributed to the wake region flow. However, in his experimental set-up, there is already an obstacle (i.e., the strut) in the wake flow which must have some influence on the phenomenon. In this sense, it is desirable to conduct another experiment in which a wake region is cleared off from obstacles. Besides the wind tunnel experiment, Hiraki conducted a free drop test of the capsule of real scale by means of a balloon. In this free flight test, he confirmed a similar unstable motion at transonic speed. In this sense, the wind tunnel experiment allowing one degree of freedom motion is enough to investigate the phenomenon. For the wake flow behind a capsule at transonic flow, an intensive study was conducted by Teramoto[8] numerically. He confirmed Hiraki's suggestion that the main cause of the phenomenon can be attributed to the wake region flow. Even though there are lots of recent intensive studies, a comprehensive understanding of the phenomenon ; i.e., not only the mechanism of enhancing the attitude motion but also the mechanism of its saturation, is not yet obtained.

In the present study, we attempt to get a comprehensive understanding of the phenomenon by means of not only a wind tunnel experiment but also a numerical simulation. For the wind tunnel experiment, we employ a set-up of the model in the wind tunnel so that the wake region is cleared off from obstacles; i.e, obstacles are avoided in the wake region near the model. In parallel to the experiment, we conduct a numerical investigation which gives us a rough but a whole picture of the flow field of which validity is verified through a comparison with the experimental results.

The outline of the present paper is as follows: The section 2 and 3 are devoted to the description of the experimental set-up and the numerical simulation technique. The result is presented in section 4 where, first, the steady aerodynamic characteristics and the flow field features, and next, the unsteady aerodynamic characteristics are discussed. Through the discussion, the model for the unsteady flow caused by the pitching motion of the model is proposed, which is utilized to estimate the dynamical part of the pitching moment acting on the body. The theoretical consideration on the unstable pitching motion is given in section 5, based on the estimated dynamical part of the pitching moment. The proposed theory gives an estimation for not only the growth rate but also the saturation amplitude of the pitching oscillation, which are compared with the experimental and numerical results. Section 6 is devoted to the discussion on the related phenomena and the concluding remarks are given in section 7.

2. EXPERIMENTAL SET-UP

The model used in the experiment is a scaled model of the reentry capsule for MUSES-C program, which is a sample return mission from an asteroid[9]. The model configuration is a blunted cone with an apex of a half angle of 45 degrees, as depicted in Fig. 1. Its diameter D and moment of inertia I are $70\,mm$ and $2.20 \times 10^{-4} kg\,m^2$, respectively. To make a wake region behind the model clear from obstacles and give the model a one-degree of freedom pitching motion, we employed a strut system depicted in Fig. 2. In this strut system, the model is supported sideways by means of a horizontal rod installed between the strut fork. The rod between the fork can rotate freely almost without friction. The center of the rod on which the model is fixed coincides with the center of gravity of the model around which the model is aerodynamically stable in a sense of static stability. The rotation angle of the rod is measured by means of a potentiometer attached to the rod. The potentiometer itself is mounted on the fork. The size of the clearance behind the model is larger than the circulation region in the wake flow. Apparently, the rod may have some influence on the wake, but the influence is expected to be more indirect than the strut system employed for Hiraki's experiment. When the wind tunnel starts, the model is fixed at a certain pitch angle θ (usually at $\theta = 0$) by means of a stopper mounted on the strut. After the wind condition becomes steady, the stopper is released and the model starts to move.

In our preliminary experiment, we have confirmed that the primary contribution of the unstable motion comes from the rear portion of the model[10]; in the experiment, only a rear portion of the model is replaced by a hemispherical configuration on which any pressure distribution could not produce any aerodynamic moment around the rod since the center of the hemisphere coincides with the rod, and no unstable motion was observed even in the condition that the unstable motion could be observed for the original configuration. Hence, in the present experiment, we concentrate on the relation between the aerodynamic effect on the rear portion of the model and the unstable motion. For this purpose, the pressure distribution of the rear side of the model was measured during the oscillation. The 4 taps for pressure measurement are allocated on the rear side of the model in line vertically; the ports A, B, C, and D in order from top to bottom, as shown in Fig. 1. The ports A and B are located in symmetric positions with the ports C and D, respectively. Inside the model, a flexible tube is installed to introduce the pressure at the tap into the pressure sensor outside. Four tubes in all are guided from inside the model into inside the rod; a pair of tubes in a right side, and another in a left side of the rod. Finally, they are connected to the pressure sensors, two pair of which are mounted on the right and left side of the strut fork, respectively. The tube inside the rod is connected directly to the pressure sensor on the strut fork, but its influence on the rod rotation is almost negligible because of its sufficient flexibility. The length between them, however, should be as short as possible in a view point of high responsibility but is around 20 cm in the present setup. Even though, in general, such a tube might deteriorate the accuracy of the pressure measurement, we have confirmed that the pitching motion does not affect the pressure measurement and the response of the measurement system can be kept up to $1\,kHz$, which is high enough compared with the frequency of the pitching motion of the model which is around $20Hz$. The pressure measurement data is recorded with a sampling rate of 1024 data per second.

The present experimental set-up was planned so that an effect of obstacles on the wake flow is minimized. However it is impossible to accomplish it completely. In fact, the effect of the horizontal rod or the side fork still exists. Hence, in order to interpret the experimental result, we must take account of their effects and, then, it is useful to know how such an obstacle in the

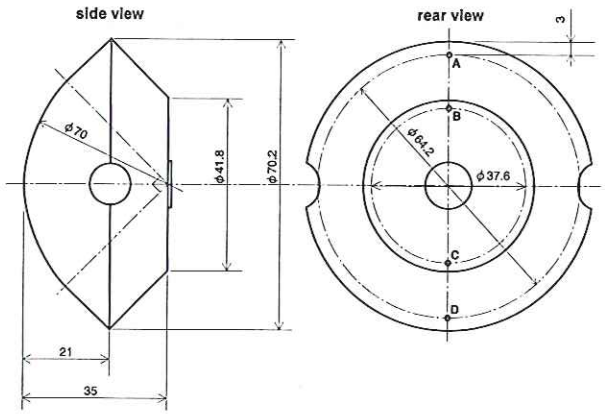

Fig. 1: Capsule model configuration for the wind tunnel.

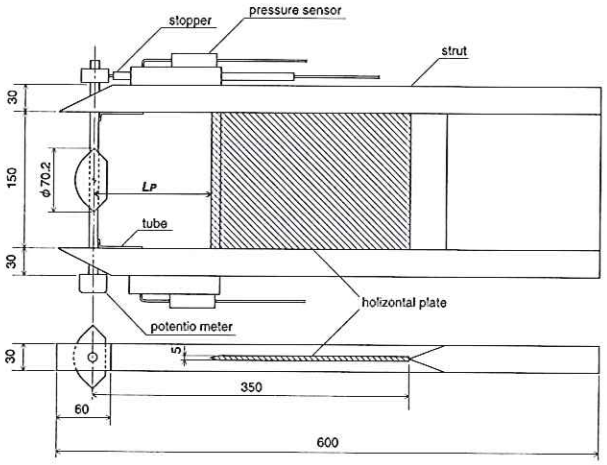

Fig. 2: Strut system to support the model in the wind tunnel.

wake region influences the phenomenon. For this purpose, a horizontal flat plate is installed between the strut fork. The horizontal plate is expected to become an obstacle which may influence the wake flow. The location of the obstacle can be variable in a following manner. That is, the distance L_p from the model center of gravity to the tip of the plate is variable while the other end of the flat plate is attached to the supporting structure. In this way, we can examine the effect of an obstacle in the wake region.

The transonic wind tunnel at ISAS was used for the experiment. The tunnel is of a blow down type having a test section of 60 cm by 60 cm, and a Mach number ranges from 0.3 to 1.3. For the experiment, the settling chamber pressure is fixed as $1.5\,kg/cm^2$. The Reynolds number based on the model diameter D is $6.7 \times 10^5 \sim 1.6 \times 10^6$.

3. NUMERICAL ANALYSIS

Since the information available from the present experiment is limited, we have conducted a numerical analysis to reinforce the information available from the experiment. Generally

speaking, it might be a tough work for the current CFD technique to predict the wake flow preciously. However it may be possible to deduct a useful information from the numerical analysis by combing it with the experimental results.

The purpose of the numerical analysis is double folded. One is to get an information regarding the steady flow field around the model fixed at a certain pitch angle. Another is to get an information regarding a unsteady flow generated by a oscillating motion of the model. For the latter purpose, we have examined the flow field generated by the model with a forced oscillation.

The governing equation used for the numerical simulation is the unsteady three-dimensional Reynolds-averaged Navier-Stokes equations with thin-layer approximation. For the numerical simulation of the steady flow field and the unsteady flow field, the governing equation is transformed into the generalized body fixed coordinate system. In the simulation of the unsteady flow due to the forced oscillation of the model, the grid system, instead of the model, rotates rigidly about the rotation axis which passes through the center of gravity of the model, vertically in the pitch plane. The numerical fluxes for the convective terms are evaluated by the SHUS scheme (Simple High-resolution Upwind Scheme)[13], which belongs to a family of the AUSM-type schemes. For the higher-order extension, the MUSCL approach[12] is used and, for the time integration, the LU-ADI method[14] is used. For the effect of turbulent flow near the body surface, the Baldwin-Lomax[11] turbulence model is employed at the limited region near the body surface. The flow Mach number ranges from 0.9 to 2.0.

4. RESULTS

4.1 Steady aerodynamic characteristics

First, we will examine a steady aerodynamic characteristics of the model, combining both the experimental and numerical results. Before going to the detail, let us see a general view of the flow field by means of a flow visualization. Since the wake flow is a key issue from a view point of the dynamic instability, we will focus on the wake flow structure. As for a flow visualization, the oil flow technique was employed. For this purpose, a vertical plate is inserted right behind the model, symmetrically inside the supporting strut fork so that the flow field in the vertical plane can be visualized. On the vertical plate, two vortices appear as shown in Fig. 3, which indicates that a vortex ring is formed behind the model as illustratively shown in Fig. 4. The result of the numerical simulation also shows the existence of such a vortex as shown in Fig. 5. In the wake, a stagnation point is clearly visible at the end of the wake region. The wake size L_w, which is defined as a distance from the base of the model to the stagnation point, depends on Mach number as shown in Fig. 6. Even though the numerical value is about half of the experimental value, both of them have a same trend; that is, the size becomes maximum at transonic speed.

Since the basic characteristics of the wake flow is a formation of vortex flow, it is anticipated that the flow adjacent to the rear side of the model is induced by the vortex. Hence we can expect the following flow characteristics. When the model is inclined (say, in a direction of head-up), the vortex at the upper part is strengthened while the lower one is weakened as shown in Fig. 4. When the upper vortex is strengthened, the vortex induces a stronger flow behind the model. Since the flow along the rear surface is dammed up against the outer edge of the model (i.e.; the conjunction rim of the front and rear part), it is expected that a pressure goes up along this direction. As shown in Fig. 7, the pressure distribution at the rear part of

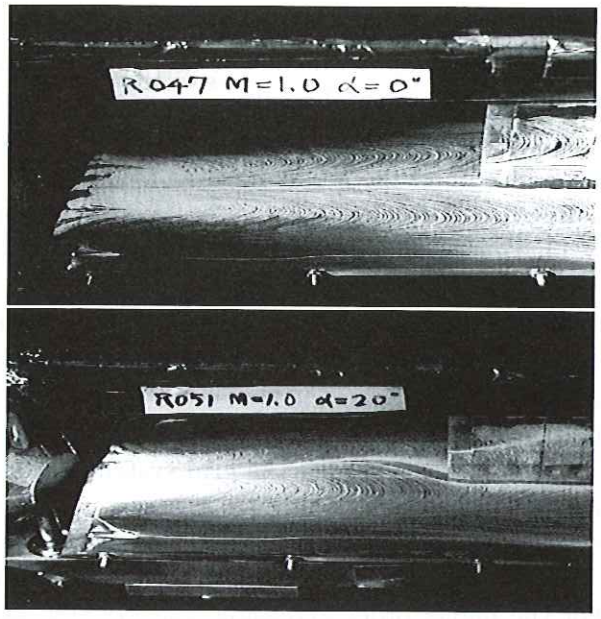

Fig. 3: Photograph for the oil flow visualization of the wake flow vortex at $\theta = 0$ (above) and 5 deg (lower).

the model shows that this is the case. That is, the variation of the pressure distribution with the pitch angle can be interpreted as being generated by the vortex behavior explained above. In the figure, upper and lower group of curves represent pressure distributions numerically obtained for the front and the rear part of the model, respectively, and a pressure coefficient C_p is defined as $(P - P_0)/(\frac{1}{2}\rho_0 U^2)$, where P_0 is a static pressure, ρ_0 a density and U a flow velocity, in a uniform flow. The coordinate z is defined vertically up-ward from the center of gravity. The pitch angle is defined as positive when the model's head is up. In the same figure, the pressure measured experimentally at the four pressure taps are shown for the rear part. Both of the experimental and numerical results show a reasonable agreement. For the front part, the pressure distribution is reasonable.

From the numerical simulation, the pitching moment generated by the pressure distribution can be calculated by integrating it around the model since the contribution of shear force is negligible. Here we will examine it, separating it into the front and rear part since they are expected to take a different part in the dynamic unstable motion. A typical characteristics of them is shown in Fig. 8. Here the pitching moment coefficient ${}^S C_m$ is defined as the pitching moment normalized by $\frac{1}{2}\rho_0 U^2 SD$, where a representative area of the model S is defined as D^2. The superscript F and R represent the front and rear part, and the right superscript S represents the pitching moment obtained for the steady flow at each fixed pitch angle. Both of them show an aerodynamically static stability. It should be noted that 1) unlike the front part, the rear part shows a strong departure from the linear behavior beyond the pitch angle around $\pm 5\, degrees$, and 2) its magnitude strongly depends on Mach number. To see the Mach number effect more clearly, we examine a magnitude of their gradients at the linear regime (i.e.; at zero pitch angle), as shown in Fig. 9. It shows that the rear part can be comparable to the front part only at transonic regime.

Now, we will see the rear side part in detail. First, let us examine the numerical results,

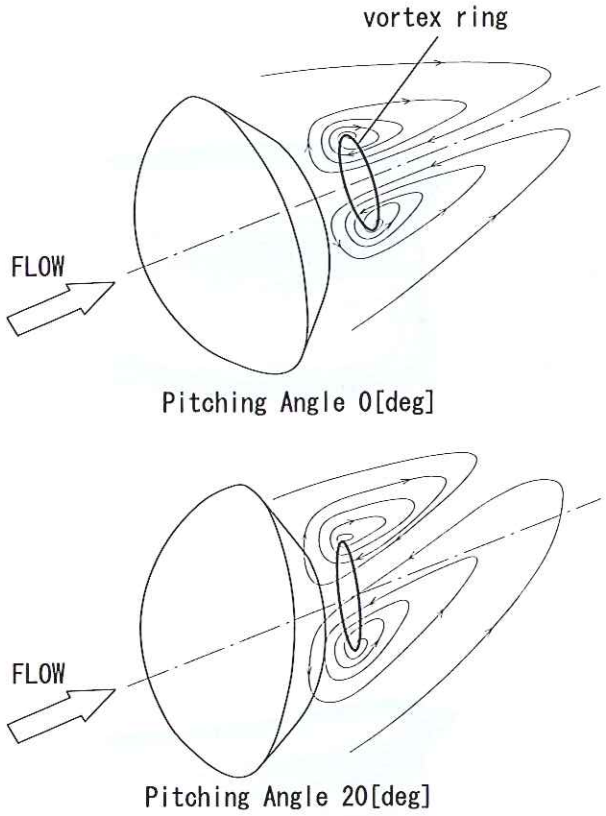

Fig. 4: Sketches of the vortical flow configuration behind the model.

especially the correlation of the local pressures and the integral pitching moment. As shown in Fig. 10, the pressure difference between the symmetric points(i.e, the outer pair comprised of the ports A, D and the inner pair comprised of the ports B, C) have a good correlation with the integral pitching moment contributed from the rear side. That is, it shows a linear behavior within a smaller pitch angle of around $\pm 5\,deg.$ and beyond it, it shows a similar nonlinear behavior. This is because the pressure difference between the symmetric points is directly proportional to the local contribution to the integral and each contribution has a similar behavior. Next let us compare the experimental and numerical result. As shown in Fig. 10, we can see a good correlation between them. This suggests that the integral pitching moment numerically obtained is somehow reliable. To examine the numerical result, the pitching moments excerted on the front and rear part of the model was measured by means of the force ballance especially invented for this purpose. The measured pitching moment excerted on the front part of the model agrees quite well with the numerical prediciton, as depcited in Fig. 12, while the measured rear part remains to quaritatively agree with the numerical prediciton as shown in Fig. 13. That is, the dependency on the pitch angle agree with the prediction while it is smaller, in one order magnitude, than the numerical prediction. Next, let us see the Mach number effect on the rear side pressure difference and pitching moment. For this purpose, we will examine a magnitude of their gradient at the linear regime. As shown in Fig. 11, they take peaks near $M = 1$ and rapidly decreases with increasing or decreasing Mach number. Again, the correlation between the pressure difference and the integral moment obtained numerically

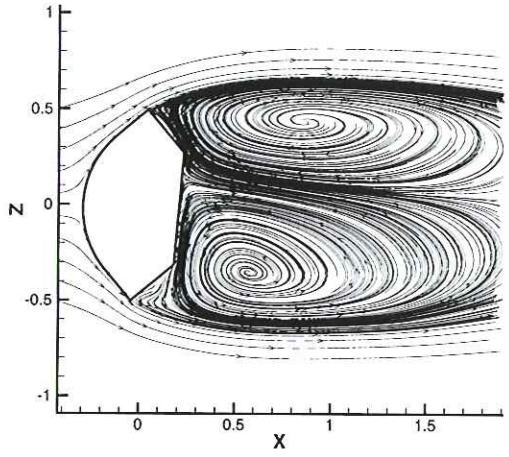

(a)

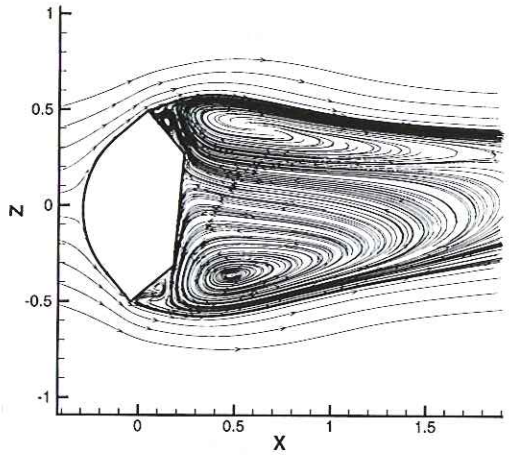

(b)

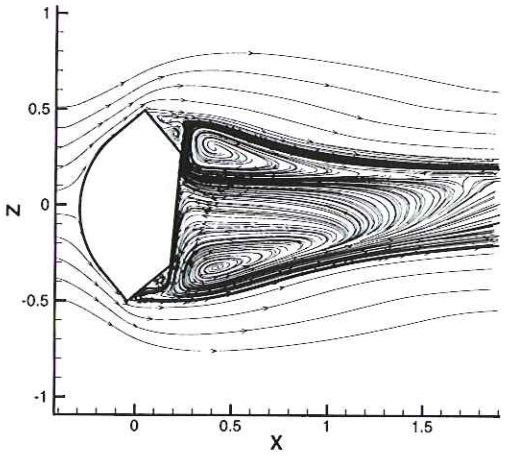

(c)

Fig. 5: Stream line plot at 5 degrees for various Mach number; 0.9 in (a), 1.1 in (b), and 2 in (c).

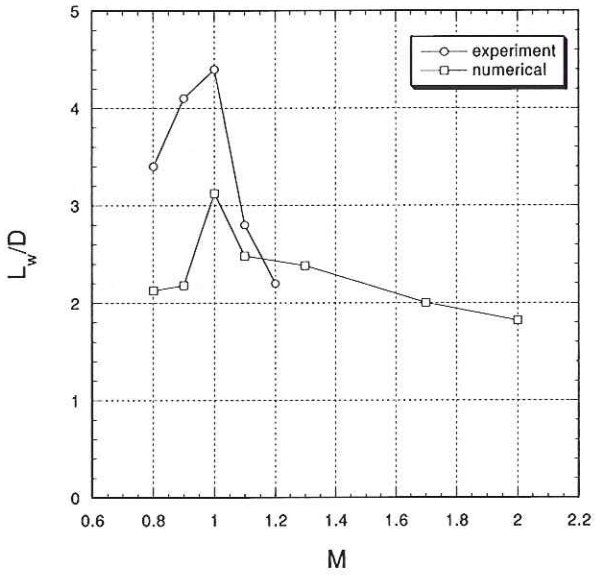

Fig. 6: Mach number effect on the size of the wake behind the model.

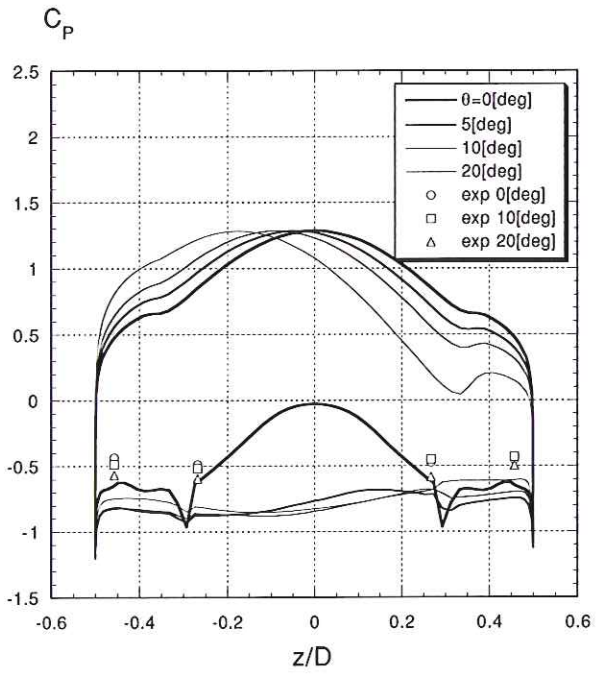

Fig. 7: Steady pressure distribution at a front and a base region of the model at fixed pitch angle.

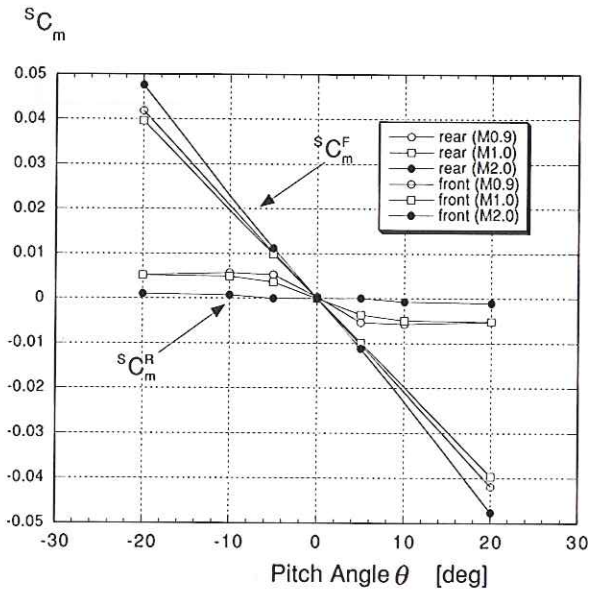

Fig. 8: Pitch angle dependence of the steady pitching moment obtained numerically for M=0.9, 1.0 and 2.0.

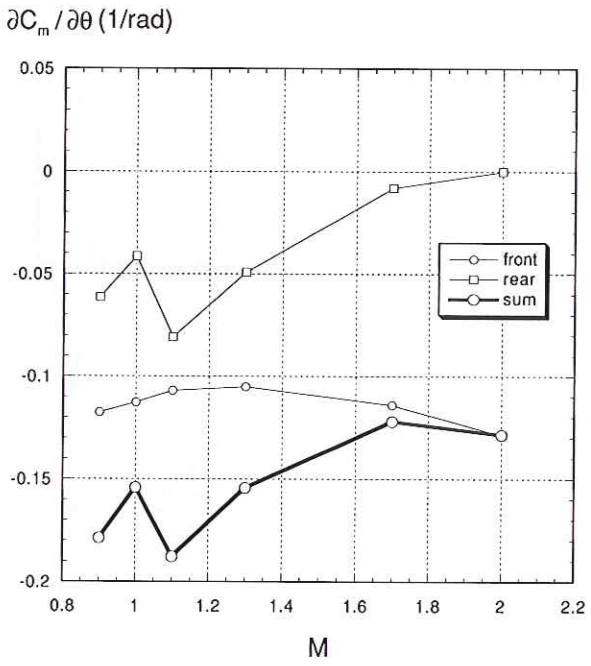

Fig. 9: Mach number effect on the gradient of the pitching moment curve at the origin, for a front, a rear side and a sum of them.

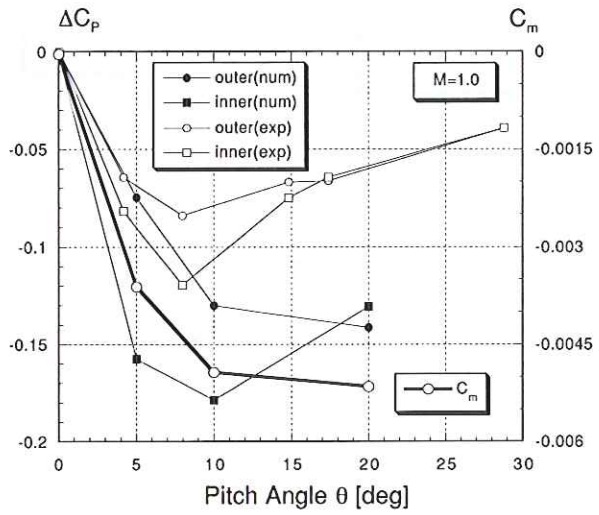

Fig. 10: Pitch angle dependency of the pressure difference and the pitching moment.

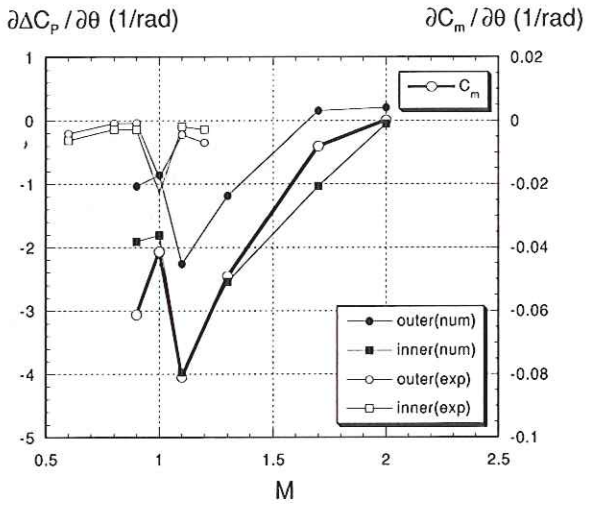

Fig. 11: Mach number effect on the gradient of the pressure difference and the pitching moment curve at the origin.

is reasonable; that is, both of them show a similar behavior. The agreement between the experimental and the numerical result is also reasonable in that the peak appears near $M = 1$ in spite of a discrepancy in the peak value. This is because 1) the strut system in the experiment may affect the wake flow and 2) the numerical simulation for the wake flow is not completely established. In any event, the agreement between them also suggests that the integral pitching moment obtained numerically is reliable. The fact that the gradient of the rear side pressure difference and the pitching moment shows a peak near $M = 1$ has a strong correlation with the flow characteristics. As discussed above, the rear side pressure distribution is governed by the vortex behavior behind the model. As shown in Fig. 5, at each Mach number, the lower vortex

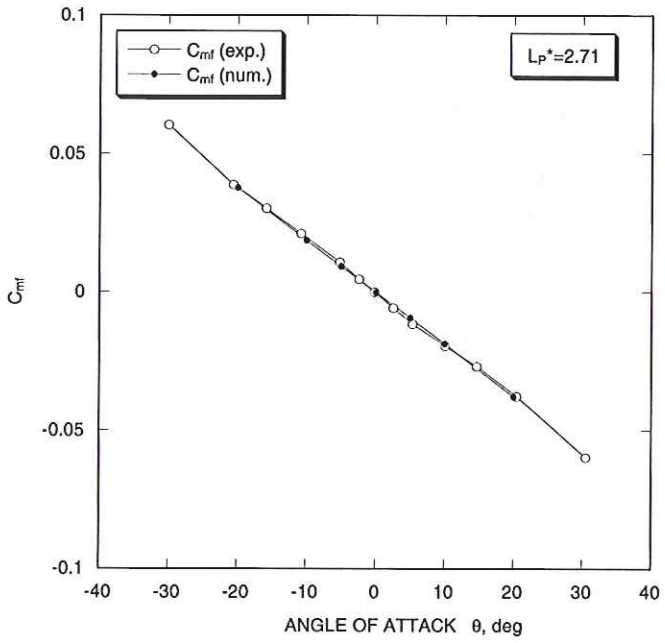

Fig. 12: Behavior of the front part of the pitching moment at $M = 1.1$.

becomes weaker for a positive pitch angle while the upper vortex, instead, becomes stronger. At the Mach number of 1.1, however, it is discernible that the difference of the strength between the upper and lower vortex becomes significant. It means that the gradient shows a peak at this Mach number since the gradient is proportional to the difference of the strength of the vortex. To get a steady state characteristic of the pressures and the pitching moment discussed above, a kind of averaging was necessary since, especially at lower Mach number, is observed the strong unsteady fluctuation of the pressures which may be attributed to the vortex shedding from the outer edge of the model. The fluctuation shows a wide spectrum centering at around 200 Hz. To represent an extent of such fluctuation, we define it as the root mean square of the fluctuation normalized by the averaged value. In Fig. 14, such a value for the pressure differences and the integral moment at the pitch angle of 5 deg. are depicted, for the experiment and for the numerical result, respectively. The value shows a sharp drop at the transonic speed while there is a significant fluctuation at subsonic speed. This is the case not only for the experiment but also for the numerical simulation.

4.2 Unsteady aerodynamic characteristics

Experiment

Unsteady aerodynamic characteristics was examined for various Mach numbers and for various length of the horizontal plate. When a stopper of the model is released, the model begins a pitching motion. The pitching motion shows various behaviors depending on the conditions; that is, in one condition it shows a complete stability and, in another condition, it shows a dynamically unstable behavior. The typical dynamically unstable motion was observed for M=1.0 and $L_p/D = 2$, for which a temporal variation of the pitch angle of the model is shown in Fig. 15. Even though the pitch angle is nearly 0 initially, it increases rapidly and reaches a

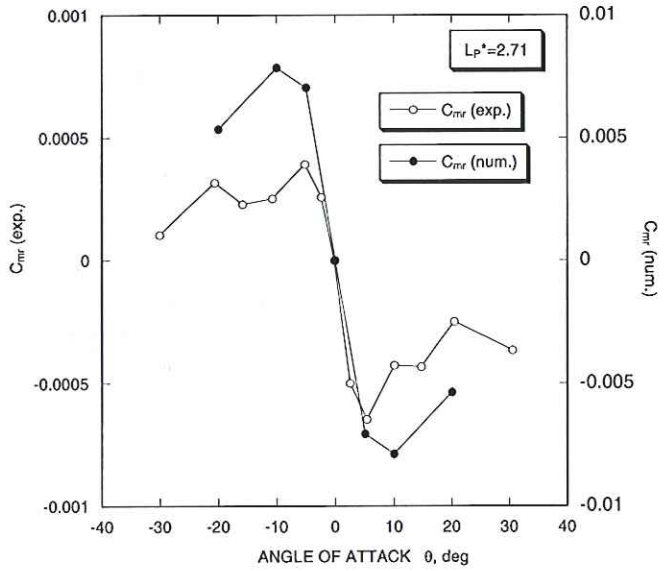

Fig. 13: Behavior of the rear part of the pitching moment at $M = 1.1$.

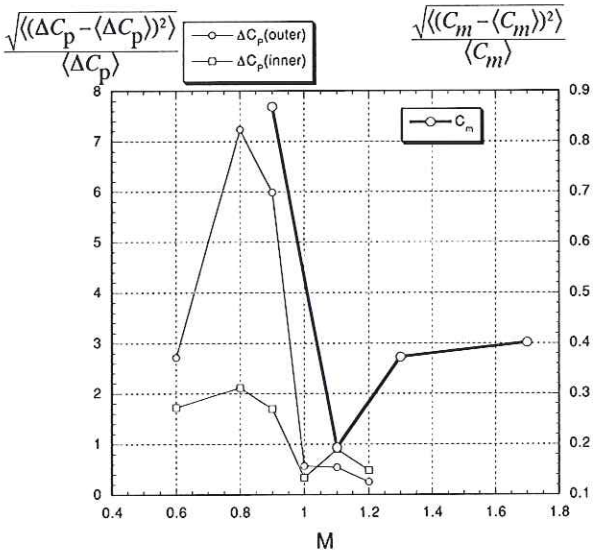

Fig. 14: Mach number effect on the fluctuation of the pressure difference and the pitching moment.

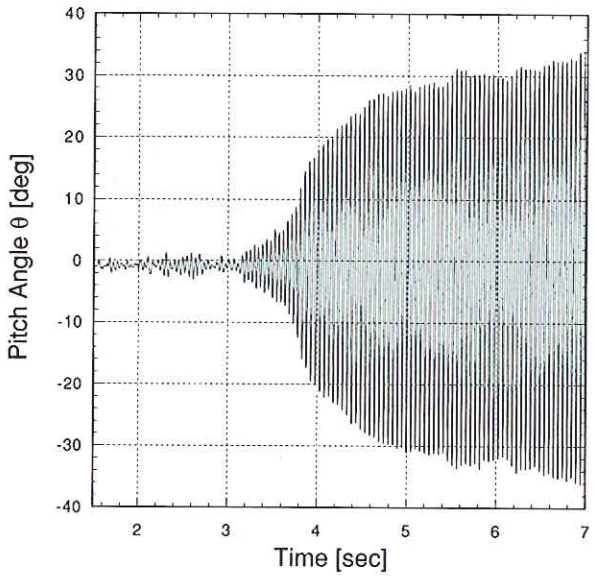

Fig. 15: Typical pitching motion at M=1.0, observed experimentally.

saturated level in which the amplitude of the pitching motion is around $\pm 30\, degrees$.

However, as noted above, the behavior of the pitching motion depends on several factors. One of them is the effect of obstacles behind the model. In this experiment, we can examine the effect of the obstacle by changing the size of the clearance behind the model, which is adjustable by the horizontal plate of variable length. The oscillation behavior of the model strongly depends on the length of the flat plate as shown in Fig. 16 where the maximum oscillation amplitude during one blow of the wind tunnel is depicted for the flow condition of $M = 1$. The oscillation amplitude becomes most significant at around $L_p/D = 2$. That is, the maximum pitch angle observed at various tip locations of the horizontal flat plate takes a peak when the tip is at a certain point behind the model while it decreases when the tip location is not only too close to but also too far away from the model. It should be noted that the pitching motion behavior in case of the tip location far away from the model is slightly different from the typical one, as shown in Fig. 17. That is, it shows an intermittent behavior. The same is the case in case of the tip location too close to the model. In this case, however, the pitching motion is almost stabilized and almost no oscillation was observed.

The Mach number also has a strong influence on the behavior of the pitching motion, which is illustrated in Fig. 18 where the maximum oscillation amplitude observed during a wind tunnel operation is depicted at the condition of $L_p/D = 2$. The oscillation amplitude shows a sharp peak at $M = 1$ while it goes down not only at subsonic but also at supersonic regime. It should be noted that the pitching motion behavior at subsonic regime is slightly different from the typical one observed at transonic regime, as shown in Fig. 19. That is, it shows an intermittent behavior like the one observed for the plate tip location far away from the model. The pitching motion behavior at supersonic regime is also different from the typical one observed at transonic regime, as shown in Fig. 20. That is, the pitching motion augmentation can be hardly observed at supersonic regime. The growth rate γ of the oscillation, which is obtained by fitting the oscillation amplitude variation to the curve of $exp(-\gamma t)$, shows a similar trend. In the figure, the representative time t_0 is defined as D/U. In case of no unstable oscillation, a damping

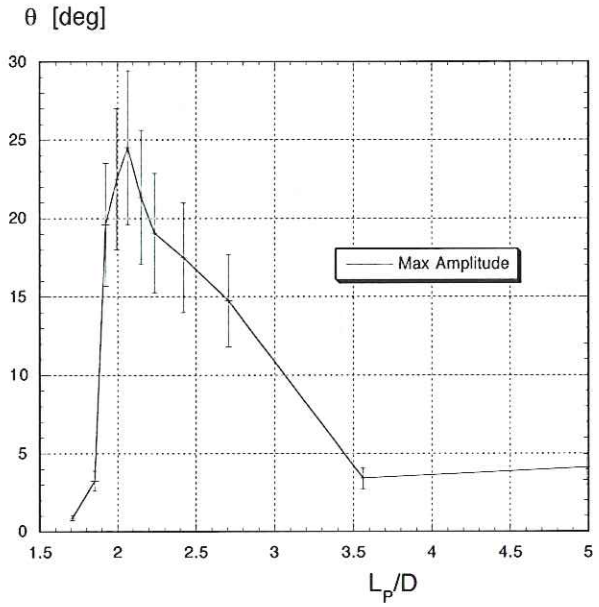

Fig. 16: Effect of the horizontal flat plate on the Maximum amplitude of the pitching oscillation.

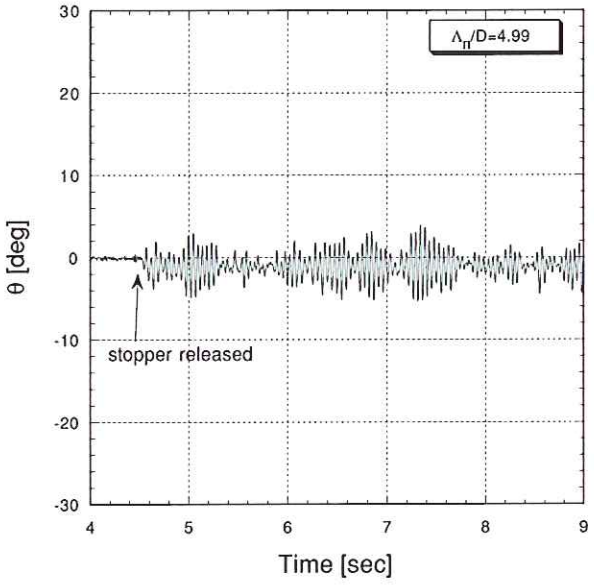

Fig. 17: Typical pitching motion without the horizontal flat plate.

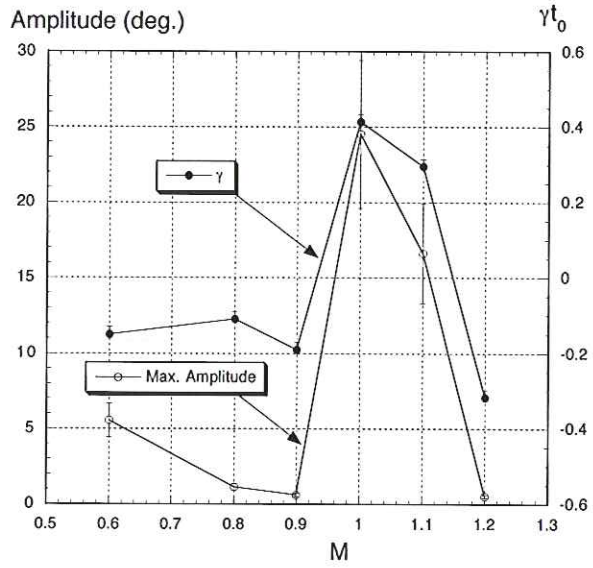

Fig. 18: Mach number effect on the maximum amplitude of the pitching oscillation and the growth rate of the oscillation.

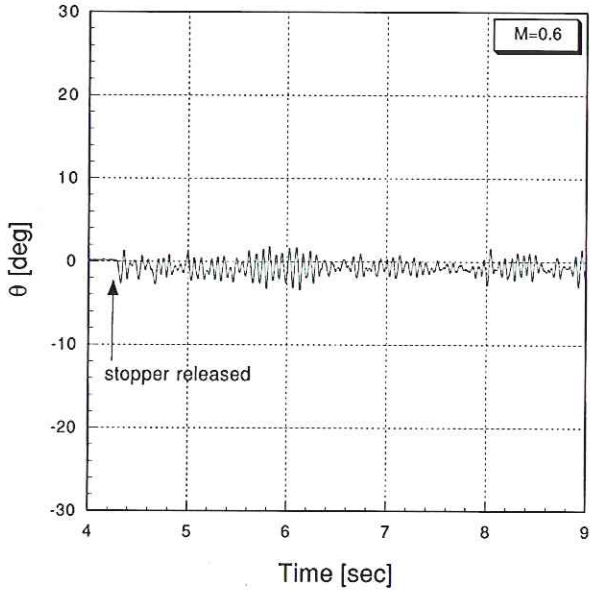

Fig. 19: Typical pitching motion at subsonic regime.

rate was measured by releasing the model deliberately from a finite pitch angle of 8 degrees, which gives the negative growth rate. Now we will see the temporal variation of the pressure distribution during the pitching motion shown in Fig. 15. Since the typical unstable motion can be classified into three phases; an early, an intermediate, and a saturation phase, we will examine it in each phases. Hereafter we will focus on the inner ports B and C, and see the relation between the pressure there and the pitching motion, since the temporal variation of

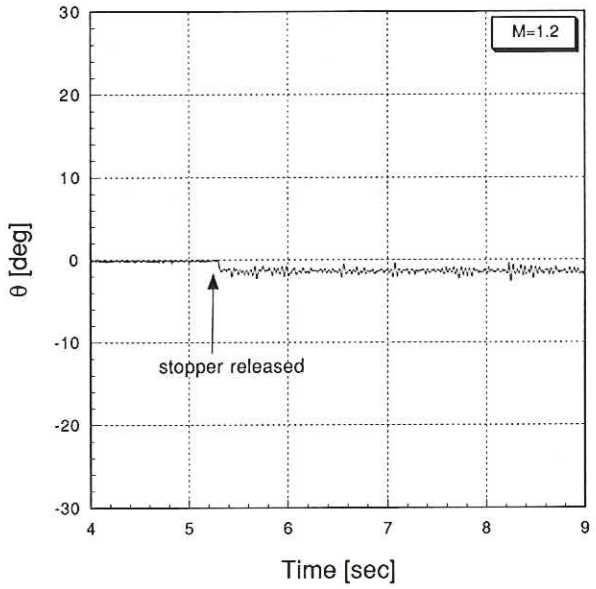

Fig. 20: Typical pitching motion at supersonic regime.

the behavior of the pressure at the ports A and B, and at the ports C and D are quite similar to each other. The typical temporal variation of the pitching motion, the pressures and the pressure difference between them are depicted in Fig. 21a, b and c, which correspond to the early, the intermediate, and the saturated phase, respectively.

At the early phase where the amplitude of the oscillation is rather small, we can see an almost sinusoidal variation of the pressure difference which synchronizes with the pitching oscillation with an approximately 180 degrees phase delay. It should be noted that this is reasonable since, in a simple harmonic oscillation, the oscillation of the pithing motion and the pitching moment inducing it completely synchronize to each other with a phase delay of 180 degrees, and, as discussed previously, the pressure difference at the symmetric points shows a good correlation to the pitching moment itself. In the present oscillating motion, however, the amplitude increases unlike the monotonous oscillation.

At the intermediate phase, the pressure difference becomes slightly concaved at the peak and the concavity becomes more significant in parallel to the increase of the amplitude of the pitching motion. At the saturation phase, this concavity becomes significant so that the sinusoidal behavior like the one observed at the early phase is no more discernible while the behavior is still periodical. Hence we can anticipate that the appearance of the concavity is related to the saturation of the pithing motion.

The behavior of the unsteady pressure difference in all the phases can be interpreted by assuming that the unsteady pressure difference at a certain pitch angle is almost the same as the one available for the steady flow at the same pitch angle. As shown in Fig. 10, the steady pressure difference shows a linear correlation with the pitch angle at a smaller pitch angle while, at a larger pitch angle, it departs from the linear correlation but rather decreases with an increasing pitch angle. If this characteristics appears even when the model oscillates, the sinusoidal behavior of the pressure difference at the early phase can be expected since, for a smaller pitch angle, the pressure difference depends on the pitch angle linearly. And, the

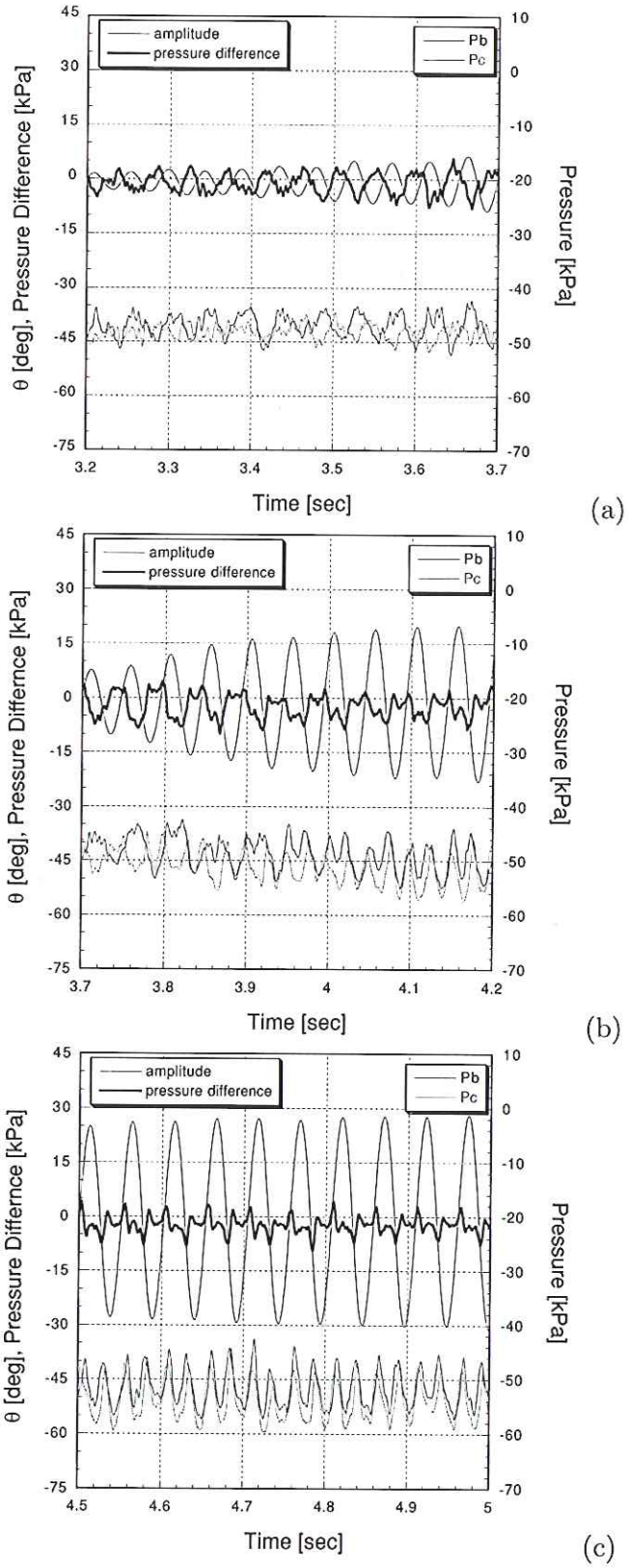

Fig. 21: Relation between the pressures at the port B, C and the pitching motion.

concavity at the intermediate and the saturation phase can be attributed to the departure from the linear dependence at a larger pitch angle.

A careful observation, however, shows that there is a slight temporal delay of the unsteady pressure difference variation from the one expected from the steady pressure difference at each pitch angle. To see this more clearly, is suitable a so-called phase plot of the pressure difference against the pitch angle. Corresponding to Fig. 21a, b and c, the phase plot is shown in Fig. 22a, b, and c, respectively. If such a temporal delay does not exist, the curve in the plot should have a single value at each pitch angle. However, as the plots show, at each pitch angle the pressure difference has 2 values instead of a single value; one for a pitch-up motion and another for a pitch-down motion. That is, it shows a hysteresis. As mentioned previously, such a hysteresis can be attributed to a temporal delay of the unsteady pressure difference variation from the one expected from the steady pressure difference at each pitch angle. To illustrate this, let us plot the following curve;

$$\begin{aligned} \theta(t) &= \sin(\omega t) \\ \Delta P &= {}^{S}\Delta P(\theta(t-\Delta t)) \end{aligned} \tag{1}$$

where ${}^{S}\Delta P$ is the pressure difference curve obtained for the steady flow as a function of pitch angle and a sinusoidal pitching motion with a frequency ω is assumed. That is, it is assumed that the pressure difference appearing on the oscillating model corresponds to the steady state pressure difference for the pitch angle at the time prior to the present time by Δt. In the plot, the oscillation motion is assumed to be a sinusoidal one, which is reasonable for the present situation. As shown in Fig. 22, the phase plot generated in this manner agrees well with the phase plot of the measured value when a certain temporal delay Δt is assumed. This is the case not only for the early phase where the steady characteristics is almost linear but also for the saturation phase where the steady characteristics shows a significant nonlinear behavior. Conversely we can determine the temporal delay Δt by fitting the thus regenerated phase plot to the measured one. This procedure is applicable not only for the inner pressure difference but also for the outer pressure difference. The temporal delay Δt_R thus obtained from the 4 pressure measurements shows a good agreement to each other. Furthermore the temporal delay Δt_R thus obtained for all the phase agrees to each other. As shown in Fig. 23, the temporal delay thus obtained slightly increases with an increasing Mach number. In the same figure, the oscillation frequency is also depicted and shows a slight decrease with a Mach number. The ratio of the delayed time against the period of the oscillation period T is almost constant but shows a slight peak at around M=0.8. It should be noted that the temporal delay is as large as about 10% of the period of the oscillation. From the discussion above, we can conclude that the pressure difference at the rear part of the oscillating model almost coincides to the steady state value at the pitch angle corresponding to the time prior to the present time by Δt_R. Since such a pressure difference variation shows a good correlation with the pitching moment variation as discussed above, we can expect that the pitching moment itself shows a similar temporal delay when the model oscillates.

Next question is how the temporal delay can be related to the flow field characteristics. To answer this question, let us consider the model in a steady flow and the situation where its pitch angle is shifted abruptly by a slight amount from the one at the steady state. Since the flow behind the model is dominated by a vortical flow, it is easily expected that a certain time is necessary for the vortical flow to adjust to a new attitude of the model. The characteristic

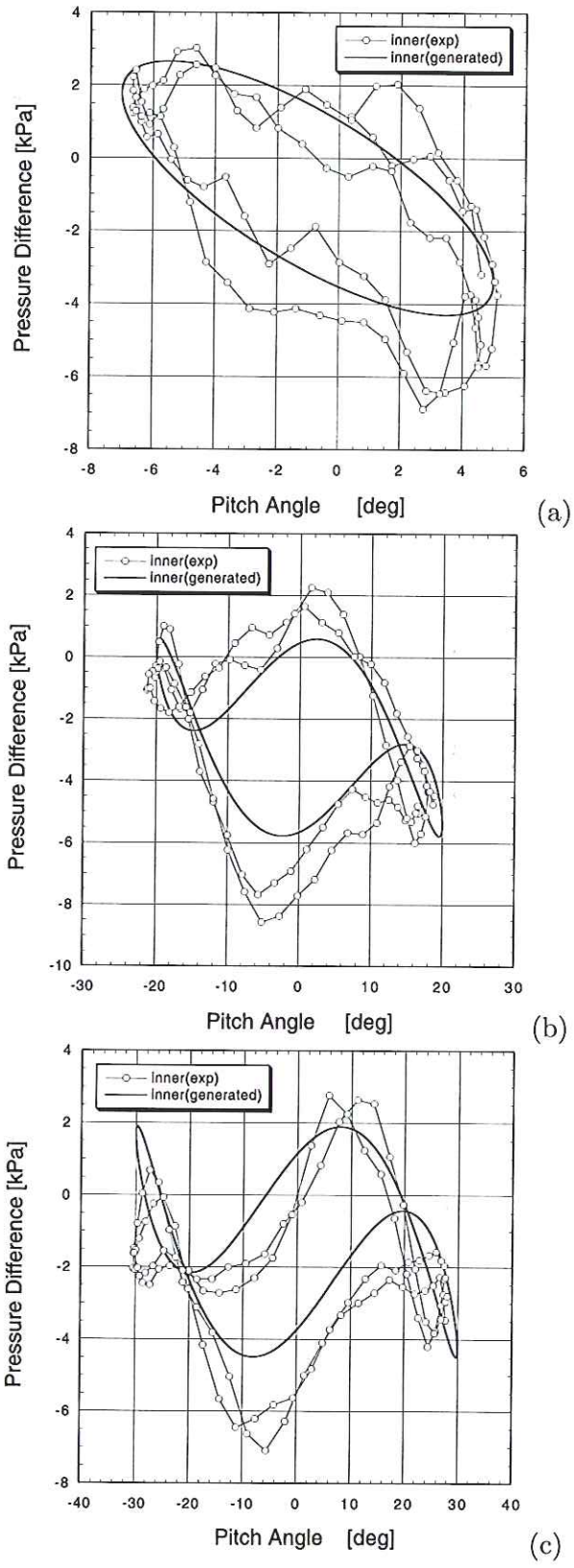

Fig. 22: Phase plot of the pressure difference. The solid line with a symbol represent the curve generated from the temporal delay model.

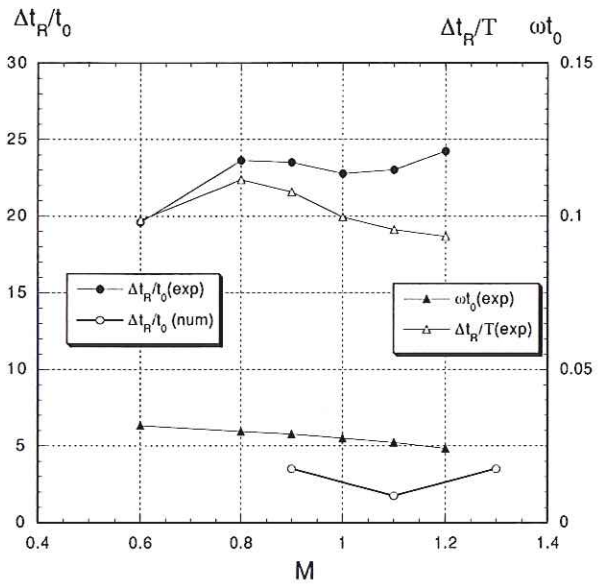

Fig. 23: Temporal delay Δt_R obtained experimentally and numerically, and the pitching motion frequency ω.

time for the adjustment should be estimated as

$$\Delta t_W = L/U_W$$

where L and U_w are the representative length and velocity at the wake region, respectively. That is, a relaxation time Δt_W is necessary for the proper pressure distribution to be formed. When the model oscillates smoothly, the relaxation time can cause that the pressure distribution of the oscillating model at a certain pitch angle remains to be the one at the time prior to the present time approximately by the relaxation time. When we assume an estimation of L as two times of the wake length L_w considering the back and forth of the disturbance from the model surface and assume $U_w = 0.5U$ for example, Δt_w becomes $16t_0$, which is almost equivalent to the experimentally observed values of around $20t_0$. Hence we can expect that the characteristic time Δt_W is equivalent to the observed temporal delay Δt_R and the origin of the delay for the pressure difference is attributed to the circulation motion in the wake flow field.

Numerical result

As for the numerical simulation of the forced oscillation, we employed parameters such as an oscillating frequency and an amplitude, in accord with the experiment not only present but also Hiraki's, which are listed in Table 1. As for the initial flow field, is employed a steady flow at the pitch angle of 0. After a few oscillation from the beginning of the calculation, almost periodic flow synchronizing with the pitching motion is obtained. The pitching moment acting on the body can be obtained by integrating the pressure distribution over the surface. The phase plot of the pitching moment against the pitch angle is shown in Fig. 24, where the front part and the rear part are shown separately for the condition of $M = 1.1$. Not only the front part but also the rear part show a hysteresis like the one discussed in the previous section. In

Table 1: Parameters for the numerical simulation.

M	0.9	1.1	1.3	1.7	2.0
θ_0 (deg.)	25	25	30	8	5
$\omega\ t_0$	0.035	0.030	0.026	0.026	0.027

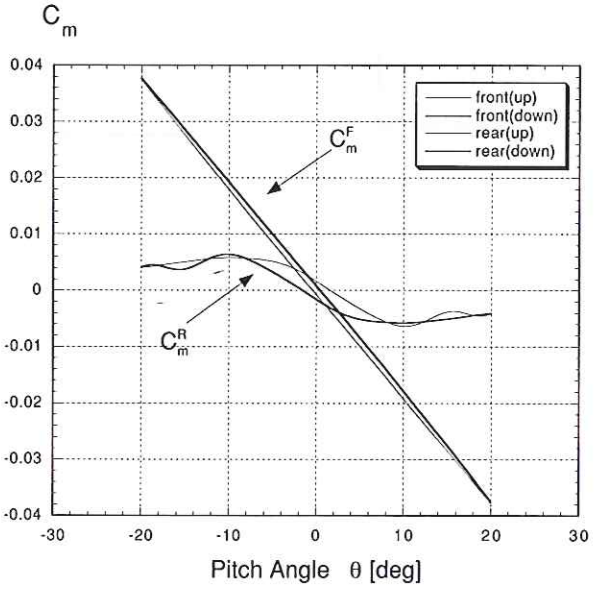

Fig. 24: Phase plot of the pitching moment against the pitch angle, at M=1.1.

the plot, the thick and thin curve correspond to pitch-down and pitch-up motion, respectively.

For the rear part, the phase mismatch (i.e, a phase delay in this case) like the one observed for the experimental result appears. In a similar manner with the one explained previously, we can extract the phase delay by fitting a set of following equations similar to eq. (1),

$$\begin{aligned} \theta(t) &= \sin(\omega t) \\ C_m &= {}^S C_m(\theta(t - \Delta t)) \end{aligned} \tag{2}$$

where ${}^S C_m(\theta)$ is the steady pitching moment as a function of the pitch angle. As shown in Fig. 23, the temporal delay thus extracted from the numerical result shows a reasonable agreement with the experimental value in that it is almost constant, but the value obtained numerically is rather smaller than the one obtained from the experimental result. For Mach number 1.7 and 2.0, the plot of the temporal delay was omitted since it becomes unreasonably large, which is caused by the fact that ${}^S C_m(\theta)$ becomes very small and the calculated value Δt becomes sensitive to the calculation error. Hence, for these Mach number, it is formidably difficult to obtain the precise value. The present experimental result suggests that the temporal delay shows a weak dependency on the Mach number and it is expected that this tendency is also the case for the higher Mach number regime. In contrast to the rear part, the phase mismatch observed for the front part shows the phase advancement. This can be easily seen from the fact that the thick curve is at the opposite side, compared with the one in the rear part. Similarly

to the rear part, we can extract the phase difference. That is, the time advancement can be obtained by fitting eq. (2) to the simulation result. In this case, however, we must assume the time advancement in contrast to the temporal delay in the case of rear part. Apparently from the figure, the phase mismatch for the front side is not as significance as the one observed for the rear part.

In either case of the time delay or advancement, when the temporal difference Δt is small enough, we can obtain a following relation;

$$\begin{aligned} C_m &= {}^S C_m(\theta(t+\Delta t)) \\ &= {}^S C_m + (\partial {}^S C_m/\partial\theta)\Delta t\dot{\theta} \\ &= {}^S C_m + \beta\dot{\theta} \\ &= {}^S C_m + {}^D C_m. \end{aligned} \tag{3}$$

where it is assumed that $\theta(t+\Delta t) = \theta(t) + \dot{\theta}(t)\Delta t$. That is, the pitching moment for the oscillating model can be expressed as a sum of a static part ${}^S C_m$ and a dynamic part ${}^D C_m$, and the dynamic part of eq. (3) can be expressed as a product of $\dot{\theta}$ and the rest β. It should be noted that, from the phase plot for the forced oscillation simulation, we can easily evaluate the extent of the dynamical part directly. That is, the pitching moment at $\theta = 0$ equals to the dynamical part itself since the static part vanishes there. And the proportional constant β can be obtained by dividing it by $\dot{\theta}$ at $\theta = 0$.

Now we attempt to predict the dynamic part in a context of the flow field. First let us consider the rear part. For the rear part, we assume that the pressure distribution is dominated by the vortex flow in the wake region and is close to the steady one appearing with a slight temporal delay, as discussed previously. The theoretical estimate for the dynamical part can be obtained from thus assumed temporal delay and the steady aerodynamic characteristics of $\partial {}^S C_m/\partial\theta$. As shown in Fig. 25, the theoretical value and the corresponding value directly obtained from the simulation shows a reasonable agreement. Here the value of $\Delta t_F/t_0 = 3$ was assumed in accord with the simulation result. That is, it shows a sharp drop at supersonic regime even though there remains a slight difference between them.

As for the front part, we consider the following flow model, in which we assume that the surface of the moving body generates a pressure wave at each instant because of the surface velocity normal to the surface and, in return, the wave generates an additional pressure on the model surface. The local pressure P caused by the wave is determined by the normal velocity V_n of the surface and is expressed as follows,

$$\begin{aligned} P &= \left(1 + \frac{2\gamma}{\gamma+1}\left(M_1^2 - 1\right)\right) P_s \\ M_1 &= \frac{\gamma+1}{4}\left(M_n + \sqrt{M_n^2 + \frac{16}{(\gamma+1)^2}}\right) \end{aligned}$$

for $V_n > 0$, and

$$\begin{aligned} P &= \left(1 + \frac{\gamma-1}{2} M_1\right)^{\frac{2\gamma}{1-\gamma}} P_s \\ M_1 &= \frac{M_n}{1 - \frac{\gamma-1}{2} M_n} \end{aligned}$$

for $V_n < 0$,

where P_s is the local pressure on the surface when no normal surface velocity exists, and M_n

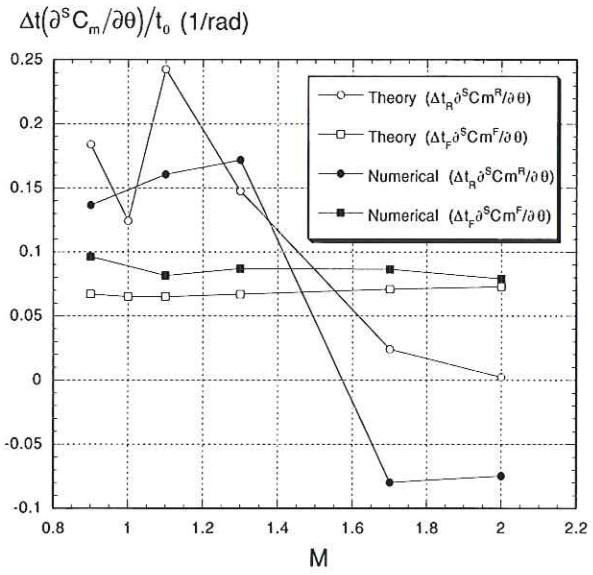

Fig. 25: Dynamical parts of the pitching moment obtained by means of the present theory and the numerical simulation.

is the Mach number corresponding to the normal velocity divided by the sonic speed at the condition without normal velocity; $M_n = V_n/C_s$. When the normal Mach number M_n is small enough like in the present case, the additional pitching moment generated according to the present model is proportional to the pitch angle rate and is calculated as,

$$\begin{aligned} {}^{D}C_m^F &= \oint P ds \\ &= -\alpha\dot{\theta} \end{aligned} \tag{4}$$

where the integration is carried out over the front surface. Comparing the expression of eq. (3) with eq. (4), we can conclude that the coefficient α is equivalent to the proportional constant $-\beta$ in eq. (4). Now let us compare the theoretical value α with the value $-\beta$ estimated directly from the numerical simulation. The value β can be obtained as a dynamical part as explained above, being divided by the $\dot{\theta}$ at $\theta = 0$. As shown in Fig. 25, the coefficient α obtained from eq. (4) and the corresponding value $-\beta$ obtained from the simulation shows a good agreement. Both of them is almost constant in every Mach number but shows a slight increase with Mach number. Therefore, we can conclude that the dynamical part of the pitching moment acting on the front part was caused by the additional pressure induced by the locally moving surface. It should be noted that, according to the present flow model, the time advancement Δt_F is only virtual in contrast to the temporal delay Δt_R which has a physical meaning.

5. THEORY FOR DYNAMIC INSTABILITY

Now we will discuss the pitching motion of the model focusing on the dynamical effect on the pitching moment. The equation of motion for the pitching motion is as follows;

$$I\frac{d^2\theta}{dt^2} = \left(\frac{1}{2}\rho U^2 SD\right) C_m. \tag{5}$$

Expressing the pitching moment as a sum of the front and rear part, eq. (5) can be rewritten as;

$$\frac{1}{\omega_0^2}\frac{d^2\theta(t)}{dt^2} = C_m^F(t) + C_m^R(t) \tag{6}$$

where $\omega_0 = \sqrt{\rho V^2 SD/2I}$ is a representative frequency. Here C_m^F and C_m^R are the contribution from the front and rear portion respectively. According to the previous discussion, each part of them can be assumed to be,

$$\begin{aligned} C_m^F &= {}^S C_m^F(\theta(t+\Delta t_F)) \\ &= {}^S C_m^F(\theta(t)) + \dot{\theta}(t)\Delta t_F\{\partial^S C_m^F(\theta)/\partial\theta\} \end{aligned} \tag{7}$$

and

$$\begin{aligned} C_m^R &= {}^S C_m^R(\theta(t-\Delta t_R)) \\ &= {}^S C_m^R(\theta(t)) - \dot{\theta}(t)\Delta t_R\{\partial^S C_m^R(\theta)/\partial\theta\} \end{aligned} \tag{8}$$

respectively. Hence eq. (6) can be rewritten as

$$\begin{aligned} \frac{1}{\omega_0^2}\frac{d^2\theta(t)}{dt^2} &= [{}^S C_m^F(\theta(t)) + \dot{\theta}\Delta t_F\{\partial^S C_m^F(\theta)/\partial\theta\}] \\ &\quad +[{}^S C_m^R(\theta(t)) - \dot{\theta}(t)\Delta t_R\{\partial^S C_m^R(\theta)/\partial\theta\}] \\ &= [{}^S C_m^F(\theta(t)) + {}^S C_m^R(\theta(t))] \\ &\quad +[\Delta t_F\{\partial^S C_m^F(\theta)/\partial\theta\} \\ &\quad - \Delta t_R\{\partial^S C_m^R(\theta)/\partial\theta\}]\dot{\theta}(t) \end{aligned} \tag{9}$$

where the first and the second term represent the static and dynamic part, respectively.

First, let us consider the case where the amplitude of the pitching motion is small enough so that we can assume the linear dependency of the pitching moment coefficient on the pitch angle;

$$\begin{aligned} {}^S C_m^F(\theta) &= -\bar{\omega}_F^2\theta \\ {}^S C_m^R(\theta) &= -\bar{\omega}_R^2\theta \end{aligned}$$

Then eq. (9) can be rewritten as;

$$\frac{1}{\omega_0^2}\frac{d^2\theta(t)}{dt^2} = -(\bar{\omega}_F^2 + \bar{\omega}_R^2)\theta + \dot{\theta}(\Delta t_R\bar{\omega}_R^2 - \Delta t_F\bar{\omega}_F^2) \tag{10}$$

The general solution for eq. (10) can be obtained as

$$\theta \propto \exp(i\omega t),$$

where

$$\begin{aligned} \omega &= \pm\omega_0\sqrt{\bar{\omega}_F^2 + \bar{\omega}_R^2} - \frac{i}{2}(\Delta t_R\bar{\omega}_R^2 - \Delta t_F\bar{\omega}_F^2)\omega_0^2 \\ &= \pm\omega_P - i\gamma. \end{aligned}$$

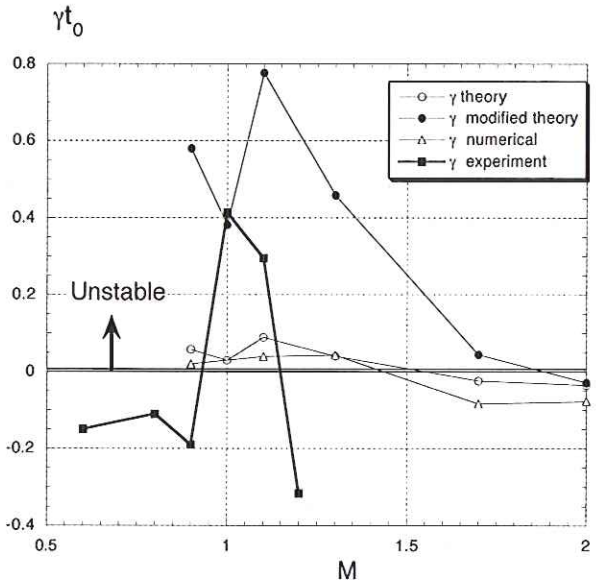

Fig. 26: Growth rate γ, obtained theoretically and numerically and experimentally. For the modified theory, the temporal delay of $\Delta t_R/t_0 = 20$ was assumed.

This solution shows an exponential growth when $\gamma > 0$ and vice versa. The growth rate of the oscillation can be expressed as

$$\frac{\gamma}{\omega_P} = \frac{1}{2}\left\{\Delta t_R \omega_P \left(\frac{\omega_R}{\omega_P}\right)^2 - \Delta t_F \omega_P \left(\frac{\omega_F}{\omega_P}\right)^2\right\} \tag{11}$$

where $\omega_R = \bar{\omega}_R \omega_0$ and $\omega_F = \bar{\omega}_F \omega_0$. It should be noted that both of the terms in the parenthesis correspond to the dynamical part of the pitching moment of the rear and the front, respectively. Since the positive γ means destabilization, the front and rear part work as a stabilizing and destabilizing effect, respectively. As shown in Fig. 25, the destabilizing factor becomes significant at transonic speed while the stabilizing factor, on the contrary, is almost constant. In all, it is expected that the growth rate becomes significant at transonic regime in contrast to at supersonic regime.

The dynamic pitching moment appearing in the linear growth rate γ can be estimated by means of not only the present theory but also the numerical simulation directly. The linear growth rate derived by both of them shows a good agreement as shown in Fig. 26. That is, both of them clearly show that the oscillation is unstable at transonic region while it is stabilized at supersonic region. This behavior of the γ value reasonably agrees with the one obtained experimentally, even though the experimental values is slightly larger than the theoretical one. The discrepancy, however, decreases when we assume the experimentally observed temporal delay t_R/t_0 of 20 instead of 3 numerically obtained. Let us consider the case where the oscillation amplitude is large enough so that the linear dependence can not be assumed. As seen from Fig. 8, the value of $\partial^S C_m^R(\theta)/\partial\theta$ becomes positive at larger pitch angles while it is negative at smaller angles. This suggests that the dynamic contribution factor in eq. (9) has a stabilizing effect at larger pitch angles and, combining a destabilizing effect at smaller angles, we can expect for the pitching motion to be in a state of limit cycle; i.e, a steady finite amplitude oscillation.

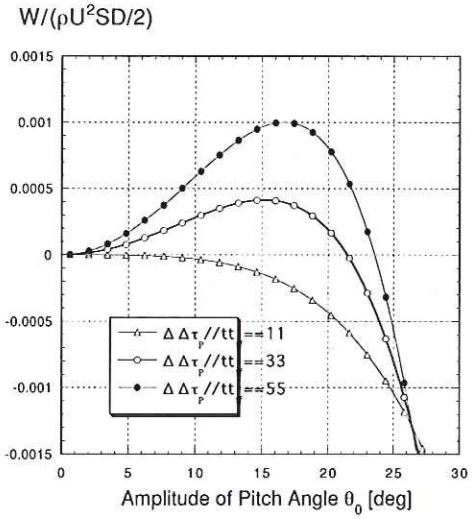

Fig. 27: Work conducted by the surrounding fluid to the body, as a function of the amplitude of the pitching oscillation.

To discuss this behavior more precisely, we will consider the following criteria for the unstable motion;

$$W = \left(\frac{1}{2}\rho U^2 SD\right) \oint C_m \dot{\theta} dt > 0 \tag{12}$$

Here the temporal integral is carried out over one period and the quantity W is a work conducted by a fluid to the body during one period. When this quantity becomes positive over several periods, the motion is considered as being unstable, because the body steadily gains an energy from the fluid. For a periodic motion without a phase mismatch with the pitching moment, this integral vanishes as a result of cancelling-out of the positive and negative contributions which come from a half period and another half period of the motion, respectively. However, as a result of the phase mismatch, this integral does not vanishes out, and the quantity W departs from zero. Now let us evaluate the quantity W assuming a sinusoidal motion with a certain amplitude and the dynamical pitching moment proposed previously based on the flow field. A typical behavior of the quantity W at transonic speed ($M = 1.1$) is shown in Fig. 27 as a function of the oscillation amplitude. It shows that the motion is unstable for an amplitude smaller than a certain critical amplitude while the motion is stabilized at an amplitude larger than the critical one. This suggests that the small amplitude oscillation is enhanced while it is kept steady at the critical amplitude. This critical amplitude can explain the saturation amplitude of oscillation observed when the pitching motion is dynamically unstable. The critical pitch angle, however, depends on the assumed temporal delay; that is, it becomes large with an increasing temporal delay. Assuming $t_R/t_0 = 3$ which was suggested by the numerical simulation, the suggested critical pitch angle becomes around 20 degrees. The critical amplitude thus obtained depends on Mach number as shown in Fig. 28. This behavior agrees with the experimental result previously shown in Fig. 18, in that the saturated amplitude shows a sharp drop at supersonic regime. In the subsonic regime, no prediction was available because of the difficulty in the simulation. However, according to the experimental

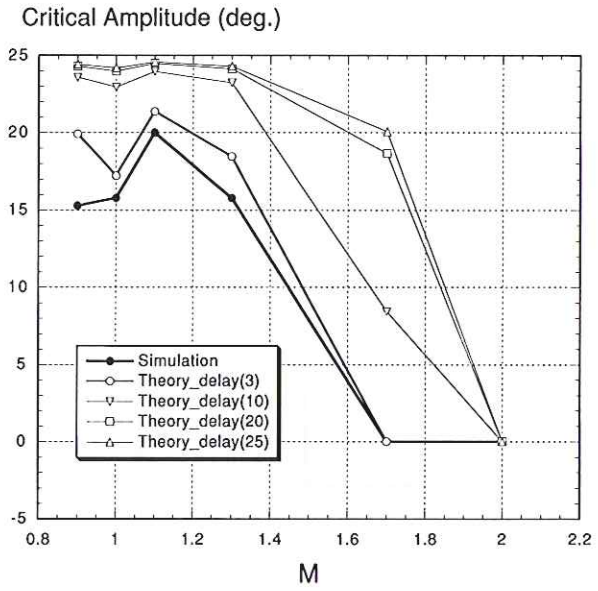

Fig. 28: Mach number effect on the saturation amplitude obtained theoretically. The simulation result represents the critical pitch angle determined by the criterion (12).

result that the pressure difference decreases suddenly at subsonic regime and to the correlation between the pressure difference and the pitching moment discussed previously, we can expect that the dynamical part of the rear side and also the linear growth rate itself decrease at subsonic regime. This suggestion agrees with the experimental fact that the maximum amplitude shows a sharp drop in the subsonic regime, like in the supersonic regime. However, unlike in the supersonic regime, the pitching motion shows an intermittent behavior in the subsonic regime. The behavior observed in the subsonic regime will be discussed in the next section. To graphically illustrate the stabilizing effect at the larger amplitude, let us rewrite the quantity W as follows;

$$W = \left(\frac{1}{2}\rho U^2 SD\right) \oint C_m d\theta$$

which is an integral along the phase plot and means a net area closed by the phase plot curve of C_m and encompassed during one period. For a smaller amplitude, the phase plot forms a single ellipsoidal shape as expected from Fig. 22. In this case, the integral gives a positive value. That is, the motion is unstable. When the amplitude becomes larger so that the linear dependency of the moment coefficient can not be applicable, additional two closed curves appear at the tips of the ellipsoidal shape, as easily expected from the experimentally observed behavior as shown in Fig. 22. Because of the opposite direction of the integral, these sides lobes give negative value for the integration and give the stabilization effect. At the critical amplitude, both the contributions cancel out to each other and W vanishes when they are summed up. This is the graphical meaning of the critical amplitude where the steady oscillation (or, the limit cycle motion) is kept. In this way, the nonlinear behavior of ${}^{S}C_m^R$ plays a crucial part for the critical amplitude.

In the discussion above, we have examined the quantity W in order to explain the existence of the limit cycle motion at a larger amplitude oscillation. However, it should be noted that

there is another way to do so. For this purpose, we can employ a theory of nonlinear equation. First, we will define the moment coefficient more concretely. Considering the pitching moment nonlinear behavior suggested by the behavior in Fig. 8, let us assume the following approximation for the rear side contribution of the pitching moment;

$$ {}^{S}C_m^R(\theta) = -\bar{\omega}_R^2\theta + b\theta^3 $$

for $b > 0$. For this pitching moment coefficient, eq. (9) becomes;

$$\begin{aligned} \frac{1}{\omega_0^2}\frac{d^2\theta(t)}{dt^2} &= -(\bar{\omega}_F^2 + \bar{\omega}_R^2)\theta + b\theta^3 \\ &\quad +\dot{\theta}\left(\Delta t_R(\bar{\omega}_R^2 - 3b\theta^2) - \Delta t_F\bar{\omega}_F^2\right) \\ &= -\omega_P^2\theta + b\theta^3 + \dot{\theta}2\gamma(1 - \frac{3\Delta t_R b}{2\gamma}\theta^2) \\ &= -\omega_P^2\theta + b\theta^3 + \dot{\theta}2\gamma(1 - \frac{\theta^2}{\delta^2}) \end{aligned} \tag{13}$$

where δ is defined as

$$ \delta = \sqrt{2\gamma/(3\Delta t_R b)} \tag{14} $$

The second term in the right hand side represents a nonlinear shift of frequency while the third term represents the nonlinear modification of the linear growth rate. When we neglect the second term for simplicity, this equation can be reduced to a nonlinear differential equation well-known as van der Pol equation of which solutions were fully investigated[15]. It is known that it contains a solution similar to the one shown in Fig. 15. That is, it shows a linear instability and a nonlinear steady oscillation which is known as a limit cycle solution. The amplitude θ_c at the steady finite amplitude oscillation becomes approximately as follows;

$$\begin{aligned} \theta_c &= 2\delta \\ &= 2\sqrt{2\gamma/(3\Delta t_R b)} \\ &= 2\sqrt{\frac{\bar{\omega}_R^2}{3b}\left(1 - \frac{\Delta t_F\bar{\omega}_F^2}{\Delta t_R\bar{\omega}_R^2}\right)} \end{aligned} \tag{15}$$

This clearly shows that the amplitude at the saturation phase strongly depends not only on the nonlinear characteristics of the steady aerodynamics ${}^{S}C_m^R(\theta)$ but also on the linear characteristics such as a linear growth rate γ and the temporal delay Δt_R. As seen from the third expression in eq. 15, when the rear part contribution of the dynamic part of the pitching moment becomes dominant in comparison with the front part, θ_c is determined only by the nonlinear characteristics of the steady aerodynamics of the rear side;

$$ \theta_c = 2\sqrt{\frac{\bar{\omega}_R^2}{3b}} \tag{16} $$

which equals to the pitch angle where the curve ${}^{S}C_m^R$ takes a local extremum at the nonlinear regime. As shown in Fig. 28, the amplitude θ_c at the limit cycle suggested by the theory shows a good agreement with the value obtained by the criterion (12) when the same temporal delay

of $3t_0$ is assumed. The critical pitch angle estimated by the present theory, however, depends on the temporal delay Δt_R which showed a slight discrepancy between the present experiment and the numerical simulation. To examine an impact of such a discrepancy, several curves with different temporal delays are also platted in Fig. 28. When the temporal delay becomes large, the critical amplitude becomes large but limited by the value (16). In any event, they shows a similar behavior, in that there is a sharp drop at supersonic regime.

As noted above, the critical pitch angle (15) depends on the linear growth rate γ, which explain why the behavior of the growth rate γ and the critical amplitude shows a similar trend as shown in Fig. 18.

6. DISCUSSIONS

Our experiment shows that, at subsonic regime, there is no monotonously unstable motion but rather an intermittent behavior is observed as typically shown in Fig. 19. As discussed previously and displayed in in Fig. 14, at this regime, we must take account of an effect of the unsteady pressure fluctuation which may be attributed to the vortex shedding. As easily expected, the existence of such a severe fluctuation in the pressure causes a corresponding fluctuation in the pitching moment and, as a result, the quantity W in the the criteria of the instability (12) becomes easily positive and negative value even for each period. Thus, there can be no more monotonous pitching motion but an intermittent behavior appears in the pitching motion, since the quantity W could change its sign randomly. It should be noted that, as shown in Fig. 26, a negative growth rate is observed experimentally even in a subsonic regime. This is because the value is observed from a deliberate damping behavior from an initial finite pitch angle. After the initial damping, however, we can observe an intermittent behavior like the one observed commonly in the subsonic regime.

As for the length of the flat plate, we have observed its strong influence on the pitching motion. For this phenomena, we can also find a similar strong pressure fluctuation effect as shown in Fig. 29. That is, it becomes minimum when the plate tip is at the certain location where the unstable motion is observed. The large fluctuation observed even when the plate is far away from the model may be caused by the supporting rod itself, and the large fluctuation observed when the plate tip is so close to the bottom of the model may be originated from the plate tip. It should be noted that the fluctuation shows a wide spectrum centering at around $200Hz$. In addition to the pressure fluctuation effect, there is another factor to enhance the unstable motion at the specific length of the flat plate. As shown in Fig. 29, we can see that one of the unstable factor $\partial^S C_m^R(\theta)/\partial\theta$ becomes significant at the specific length where another factor, that is, the unsteady pressure fluctuation becomes minimum. But when the flat plate is too close to the model, it becomes dramatically small. Considering both the effects, it is reasonable that the unstable motion was observed at a certain size of the horizontal flat plate.

7. CONCLUDING REMARKS

In the present study, we attempted to get a comprehensive understanding of the dynamically unstable pitching motion phenomenon by means of not only a wind tunnel experiment but also a numerical simulation. We can summarize the results as follows;

(1) Both experimentally and numerically, the dynamically unstable motion was observed. The behavior of the unstable motion strongly depends on Mach number. At transonic speed, the unstable motion appears most significantly and reaches a saturated amplitude

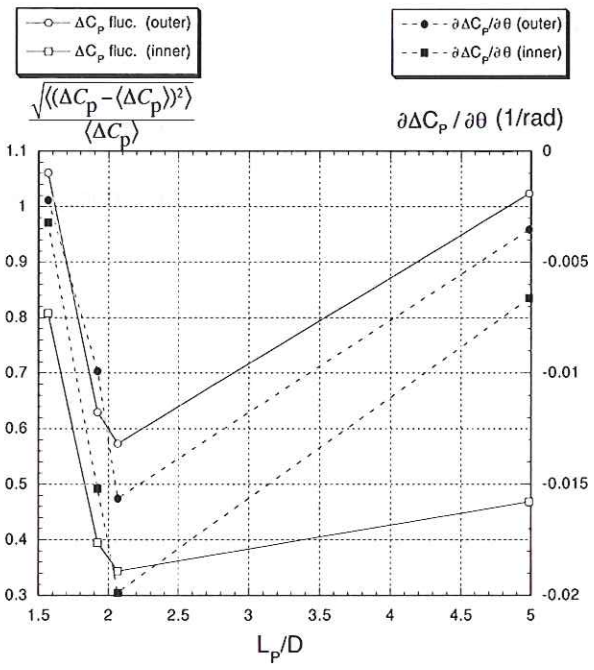

Fig. 29: Horizontal flat plate effect on the normalized pressure fluctuation and a gradient of pressure difference at the port B and C

oscillation phase. At supersonic speed, no such motion is observed. At subsonic speed, rather intermittent and weak unstable motion was observed.

(2) Combining both the experimental and numerical results, we clarified the relation between the oscillating motion of the model and the pitching moment variation at the rear part of the model and at the front, separately. Based on this, the flow model for the dynamical part of the pitching moment was proposed, which is based on the flow field characteristics for the rear and front part, separately: For the rear part, the dynamical part of the pitching moment can be estimated, based on the steady pitching moment behavior of the model assuming a temporal delay which is due to the circulation motion at the wake region behind the model. For the front part, it can be estimated by taking into account of the pressure wave induced by the model motion.

The present flow model shows a good agreement with the numerical simulation result.

(3) Based on the dynamical part of the pitching moment thus obtained, we proposed a theory for a possible mechanism of the unstable motion of the capsule body. According to the theory, the growth rate of the instability is expressed as a sum of the destabilizing factor caused by the rear part and the stabilizing factor caused by the front part. The growth rate becomes a significant destabilizing value at transonic flow regime while it becomes a stabilizing value at supersonic flow regime. This behavior completely agrees with the behavior observed experimentally and numerically.

(4) When the motion is dynamically unstable, the oscillation is enhanced up to a critical saturation amplitude and a limit cycle motion appears. The theory also enables us to

estimate the critical oscillation amplitude, whose value agrees well with the experimental observation over a Mach number ranging from a transonic to supersonic regime.

(5) At subsonic regime, the pressure fluctuation possibly caused by a vortex shedding from the outer edge of the capsule body becomes especially significant and has a strong influence on the behavior of the unstable motion in that an intermittent behavior appears.

REFERENCES

Wright, B.R., and Kilgore, R. A., "Aerodynamic Damping and Oscillatory Stability in Pitch and Yaw of Gemini Configurations at Mach Numbers form 0.50 to 4.63", NASA Technical Note NASA TN D-3334, March 1966.

Sammonds, R. I., "Dynamics of High-Drag Probe Shapes at Transonic Speeds", TN D-6489, 1971.

Sammonds, R.I., and Kruse, R. L., "Viking Entry Vehicle Aerodynamics at M=2 in air and some preliminary test data for flight in CO_2 at M=11", NASA Technical Note NASA TN D-7974, June 1975.

Yoshinaga, T., Tate, A., Watanabe, M., and Shimoda, T., "Orbital Re-Entry Experiment Vehicle Ground ant Flight Dynamic Test Result Comparison", Journal of Spacecraft and Rockets, Vol. 33, No. 5, 1996, pp. 645-642.

Berner, C., and Winchenbach, G.L., "A Numerical and Experimental Investigation of Generic Space Probes", AIAA Paper 98-0798, Jan. 1998.

Chapman, G. T., and Yates, L. A., "Dynamics of Planetary Probes: Design and Testing Issues", AIAA Paper 98-0799, Jan. 1998.

Hiraki, K., "Experimental study on dynamic instability of the capsule type vehicle" PhD thesis, University of Tokyo, 1997, in Japanese, or, Hiraki, K., Inatani, Y., Ishii, N., Nakajima, T. and Hinada, M.", Dynamic Stability of MUSES-C Capsule", 21st International Symposium Space Technology and Science, May 1988, ISTS-98-d-33.

Teramoto, S. and K. Fujii, "Computational Study of the Flow Field behind Blunt Capsules at Transonic Speeds", AIAA-99-3414, 1999, and Teramoto, S., Hiraki, K., and Fujii, K., "Numerical Analysis of Dynamic Stability of a Reentry Capsule at Transonic Speeds", AIAA paper 98-4451, June 1998.

Kawaguchi, J., A. Fujiwara and S. Sawai, "Sample and Return Mission from Asteroid Nereus VIA Solar Electric Propulsion", Acta Astronautica Vol.38 No.2 pp.87-101, 1996.

Nakajima, Y., "An Experimental Study on Dynamic Instability of Blunted Body at Transonic Speed", Mater Thesis, 1999.

Baldwin, B.S. and Lomax, H., "Thin Layer Approximation and Algebraic Model for Separated Turbulent Flows", AIAA Paper 78-257, 1978.

Anderson, W.K., Thomas, J.L., and van Leer, B., "Comparison of Finite Volume Flux Vector Splitting for the Euler Equations", AIAA Paper 85-0122, 1985.

Shima, E. and Jounouchi, T., "Role of Computational Fluid Dynamics in Aeronautical Engineering (No. 12) -Formulation and Verification of Uni-Particle Upwind Schemes for the Euler Equations-", NAL SP-27, pp. 255-260, 1994.

Obayashi, S., Matsushima, K., Fujii, K. and Kuwahara, L., "Improvements in Efficiency and Reliability for Navier-Stokes Computations using the LU-ADI Factorization Algorithm", AIAA Paper 86-338, 1986.

Tokuoka, T., "Basic Theory of Vibration for Engineering", Science Co. Tokyo, 1985 (in Japanese).